

# Polarization-entangled quantum frequency comb from a silicon nitride microring resonator


Wenjun Wen<sup>1</sup>, Wenhan Yan,<sup>1</sup> Chi Lu,<sup>1</sup> Liangliang Lu,<sup>1,2</sup> Xiaoyu Wu,<sup>1</sup> Yanqing Lu,<sup>1</sup>  
Shining Zhu,<sup>1</sup> and Xiao-Song Ma<sup>1,3,4,\*</sup>

<sup>1</sup>*National Laboratory of Solid-state Microstructures, School of Physics, College of Engineering and Applied Sciences, Collaborative Innovation Center of Advanced Microstructures, Nanjing University, Nanjing 210093, China*

<sup>2</sup>*Key Laboratory of Optoelectronic Technology of Jiangsu Province, School of Physical Science and Technology, Nanjing Normal University, Nanjing 210023, China*

<sup>3</sup>*Synergetic Innovation Center of Quantum Information and Quantum Physics, University of Science and Technology of China, Hefei, Anhui 230026, China*

<sup>4</sup>*Hefei National Laboratory, Hefei 230088, China*

 (Received 16 August 2023; revised 1 November 2023; accepted 5 December 2023; published 18 December 2023)

Integrated microresonator facilitates the realization of quantum frequency comb (QFC), which provides a large number of discrete frequency modes with broadband spectral range and narrow linewidth. However, all previous demonstrations have focused on the generation of energy-time or time-bin entangled photons from QFC. Realizing polarization-entangled quantum frequency comb, which is a useful resource for the fundamental study of quantum mechanics and quantum information applications, remains challenging. Here, we demonstrate a broadband polarization-entangled quantum frequency comb by combining an integrated silicon-nitride microresonator with a Sagnac interferometer. With a free spectral range of about 99 GHz and a narrow linewidth of about 190 MHz, our source provides 22 polarization-entangled photon pairs with frequency covering the whole telecom C-band. The entanglement fidelities for all 22 pairs are above 81%, including 17 pairs with fidelities higher than 90%. Our demonstration paves the way for employing the polarization-entangled quantum frequency comb in quantum network using CMOS technology as well as standard dense wavelength division-multiplexing technology.

DOI: [10.1103/PhysRevApplied.20.064032](https://doi.org/10.1103/PhysRevApplied.20.064032)

## I. INTRODUCTION

Entangled photons play a crucial role in the fundamentals of physics [1–7] and have practical applications in quantum information science, such as quantum communication and quantum cryptography and so on [8–12]. In particular, entangled photons are used to share secret cryptographic keys between distant parties with quantum key distribution (QKD) protocols. One can combine various degrees of freedoms (DOFs) of photons, which has great potential to expand towards higher dimensionality [13,14]. Quantum networks [15–18] (QNs) with high efficiency and scalability in real-world scenarios are expected to be realized with entangled photons.

Recently, with advancements of integrated optics technologies, such as flexible dispersion engineering, high-quality ( $Q$ ) factor, small-mode volume and compatible with the CMOS fabrication process, optical

microresonators [19] become robust, scalable, and reconfigurable devices for quantum optical applications. Based on spontaneous four-wave mixing (SFWM) using  $\chi^3$  nonlinearity [20,21], microresonators have been used to generate energy-time [18,22–24], time-bin [25,26], and frequency-bin [27,28] entangled photons. Meanwhile, due to the inherent multiresonant mode properties of microresonators, integrated cavity-enhanced devices can directly generate quantum frequency combs (QFCs) without the need for subsequent periodic filtering [29–31]. In a microresonator, the SFWM efficiency for generating photon pairs is proportional to  $Q^3$  [32]. However, for QKD protocol using phase or time-bin encoding, a higher  $Q$  factor leads to a long photon coherence time and requires a large difference in interferometer arm length, which places stringent requirements on maintaining interferometric phase stability [33].

Polarization entanglement is easy to control and analyze, and has mature automatic polarization feedback system, which is a common choice for QKD [34,35]. One way to obtain polarization entanglement is the Sagnac

\*Xiaosong.Ma@nju.edu.cn

interferometer [36–43], in which two pump beams, one clockwise and one counterclockwise, travel along the same pathway without active phase stabilization between the different directions. In this work, we use a microresonator placed in a Sagnac loop to realize a polarization-entangled QFC.

We demonstrate the generation of broadband polarization-entangled QFC in a Sagnac configuration using SFWM on a dispersion-engineered silicon-nitride microring resonator (MRR). With a total of 22 parallel pairs of frequency channels (limited by the bandwidth of our programmable filter system), a free spectral range of approximately 99 GHz and a linewidth of approximately 190 MHz, our source generates photon pairs in a spectral range of approximately 38 nm, covering the whole telecom C-band. Long-term operation of our source is ensured by temperature control and feedback control of the high- $Q$  MRR. By analyzing the photonic noise inside and outside the ring, we obtain an effective photon-pair generation bandwidth of approximately 3 THz. We show that, our source maintains entanglement fidelity above 81% for all 22 pairs of frequency channels, including 17 pairs with fidelities above 90%. Our demonstration suggests that a multimode polarization-entangled biphoton QFC generated by integrated MRR in a Sagnac interferometer can contribute to a promising platform for the realization of multiuser QNs using a commercially available dense wavelength division-multiplexing (DWDM) fiber optical communication network and interfacing solid-state quantum memories at telecommunication wavelengths [44].

## II. EXPERIMENTAL SETUP

The schematic diagram of our experimental setup is shown in Fig. 1. Our quantum light source is based on an integrated  $\text{Si}_3\text{N}_4$  MRR (Ligentec AN800) placed at the center of a Sagnac loop constructed with fiber and bulk optical elements. A cw pump laser (Santec TSL570) at 193.5 THz (1549.3150 nm) is polarized and then coupled into a free-space Sagnac interferometer. A three-port circulator (CIR) placed in front of the loop is used to transfer the pump from port 2 into the loop and to output the residual pump and generated photons through port 3. Multiple DWDMs are cascaded to form the pre- and postfilters used to remove the amplified spontaneous emission of the pump and the residual pump before and after the CIR, respectively.

As shown in Fig. 1(a), the Sagnac configuration consists of a polarization beam splitter (PBS), an optically packaged SiN MRR chip and several wave plates. The pump incident on the PBS is diagonally polarized and thus split into two orthogonally polarized components  $|H\rangle_{p,\odot}$  and  $|V\rangle_{p,\odot}$ , with horizontally polarized photons propagating counterclockwise and vertically polarized pump photons propagating clockwise. The MRR is designed to

be pumped bidirectionally with the vertical polarization mode  $|V\rangle$ . To achieve this, wave plates are used to adjust the polarization of these two components before they are coupled into the chip. The clockwise component remains vertically polarized  $|V\rangle_{p,\odot}$ , while the counterclockwise component is rotated by  $90^\circ$  ( $|H\rangle_{p,\odot} \rightarrow |V\rangle_{p,\odot}$ ).

Within the MRR, vertically polarized pump photons are converted into vertically polarized photon pairs through SFWM, i.e.,  $|V\rangle_p |V\rangle_p \rightarrow |V\rangle_s |V\rangle_i$ . The clockwise propagating photon pair  $|V\rangle_{s,\odot} |V\rangle_{i,\odot}$  are then rotated by  $90^\circ$  to  $|H\rangle_{s,\odot} |H\rangle_{i,\odot}$ , while the counterclockwise propagating photon pairs  $|V\rangle_{s,\ominus} |V\rangle_{i,\ominus}$  remain unrotated. Here, the subscripts  $s$  and  $i$  denote signal and idler photons, respectively. Photon pairs generated in clockwise and counterclockwise directions are combined by PBS and exit from the Sagnac interferometer into the input spatial mode. Meanwhile, QFC formed by frequency-entangled photon pairs, i.e., a biphoton QFC, is generated inside the MRR. In the Sagnac interferometer, clockwise and counterclockwise QFCs are generated by the same MRR, ensuring perfect spectral overlap between them. Finally, we obtain a polarization-entangled QFC with the following states [43]:

$$|\psi\rangle = \frac{1}{\sqrt{2}} (|H\rangle_s |H\rangle_i + e^{i\theta} |V\rangle_s |V\rangle_i) \otimes \frac{1}{\sqrt{M}} \left( \sum_{m=1}^M |\omega\rangle_{s,m} |\omega\rangle_{i,m} \right), \quad (1)$$

where  $\theta$  is an unknown but constant phase, and we compensate for this undetermined phase using a sandwiched QWP-HWP-QWP setup, i.e., orienting all QWPs at  $45^\circ$  and rotating the HWP [45,46]. And  $|\omega\rangle_{s(i),m}$  represents the state of the signal (idler) photon at frequency pair index  $m$  ( $m = 1, 2, \dots, M$ ).

The photons leaving port 3 of the CIR contain both the two generated photons and the residual pump, which are separated by the postfilter with a total pump rejection of approximately 115 dB. The filtered pump is detected by a power detector (PD), which monitors the resonance information of the MRR with respect to the pump. The PD signal is used, in conjunction with the integrated microheater [47] electrically driven by a current source (NI 9266), to actively stabilize the resonance of the MRR via thermoelectric tuning.

A C-band wavelength selective switch (WSS) [46] is used to demultiplex the polarization entangled QFC and provide additional pump rejection. To characterize the photon-pair generation, the WSS is configured as a dual bandpass filter to demultiplex signal and idler photons, and send each directly to a detector. The separated signal and idler photons are then sent to two polarization analysis modules (PAMs) for quantum state tomography (QST) [48]. It can also be programmed as a single-channel

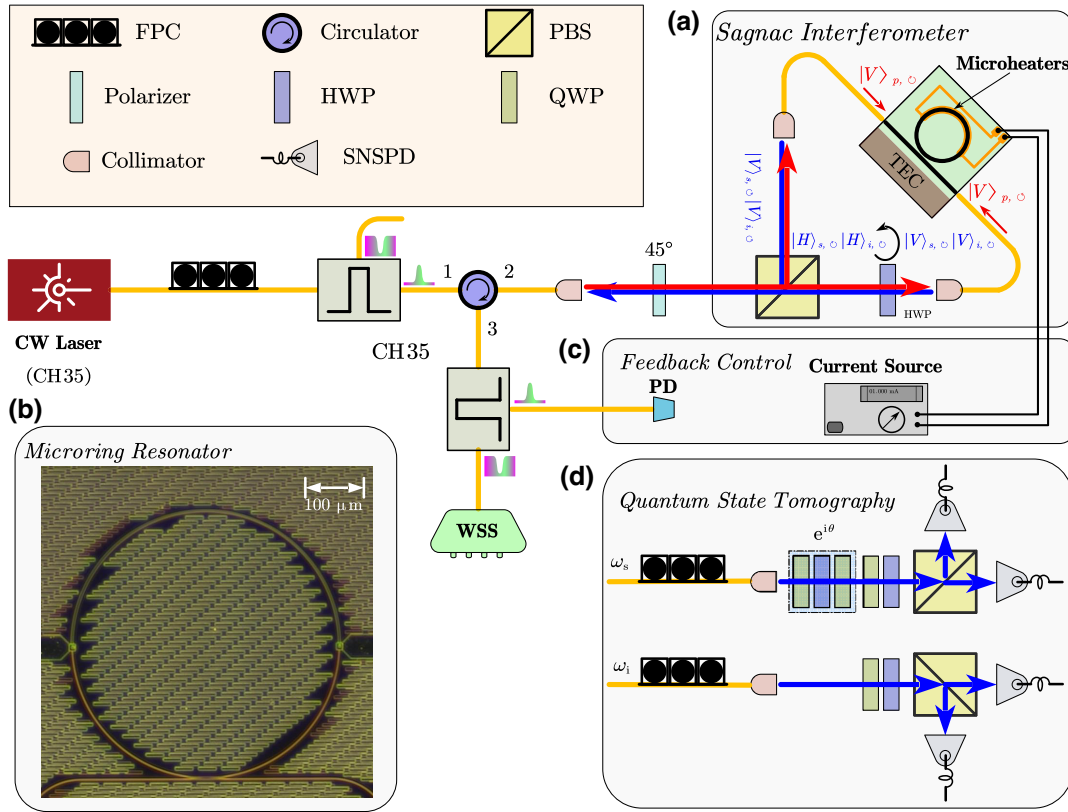


FIG. 1. Experimental setup for the generation and characterization of the polarization-entangled QFC. (a) Polarization-entangled QFC is generated in a Sagnac configuration, with an integrated silicon-nitride microring resonator at the center of the loop. Wave plates are simplified here. The chip is mounted on a copper plate whose temperature is controlled with high precision ( $<0.001^\circ\text{C}$ ) by a thermoelectric cooler and a negative temperature coefficient (NTC) thermistor. (b) Optical microscopy image of the MRR and the integrated microheater. (c) The cavity resonance is stabilized by using the integrated microheater and feedback control module. (d) Quantum state tomography is performed by the polarization analysis modules. CW, continuous wave; FPC, fiber polarization controller; CIR, circulator; PBS, polarization beam splitter; HWP, half-wave plate; QWP, quarter-wave plate; TEC, thermoelectric cooler; PD, power detector; WSS, wavelength selective switch; SNSPD, superconducting nanowire single-photon detector.

tunable bandpass filter, which is used to obtain the single-photon spectrum and to analyze the sources of noise.

### III. MRR-BASED BROADBAND POLARIZATION ENTANGLEMENT SOURCE

The radius of our MRR is about  $230\ \mu\text{m}$ , while its waveguide cross section is about  $0.8 \times 1.6\ \mu\text{m}^2$ . Inverted tapers are designed to couple light in and out of the chip, and are end coupled to ultrahigh numerical aperture (UHNA7) fiber arrays, with UV glue curing in between. The measured fiber-chip-fiber insertion loss is about 6 dB, including propagation loss. The MRR under test has an average FWHM of 190.41 MHz and an average  $Q$  factor of about  $1.03 \times 10^6$ , with a free spectral range (FSR) of 99.03 GHz (refer to Appendix A for details).

When using microresonators with high-quality factors and small mode volumes, thermal-induced phenomena such as hysteretic wavelength response [49] shows up. The hysteresis behavior broadens the cavity lineshape, but at

the same time makes it easier for the microresonator to be out of resonance. As shown in Fig. 1(c), we developed the feedback control based on the transmitted pump power and the integrated microheater, combined with the high-precision temperature control of the chip, to ensure the long-term stable operation of the source. Refer to Appendices B–D for more information.

The frequency correlated photon pairs are spatially separated by a programmable WSS, and each sent to a PAM consisting of a fiber polarization controller (FPC), a quarter-wave plate, a half-wave plate, a polarization beam-splitter cube and two SNSPDs. To map the  $|H\rangle/|V\rangle$  basis of the source to the  $|H\rangle/|V\rangle$  basis of the PAM, the FPC is used to compensate for the polarization rotation that occurs during transmission between the source and the QWP due to the random birefringence effect of the single-mode fiber. The sandwiched QWP-HWP-QWP setup placed in the signal path is then used to compensate for the remaining phase between  $H$  and  $V$ . We set both QWP to  $45^\circ$  with respect to horizontal, and then rotate the HWP in the

diagonal-antidiagonal ( $|D\rangle/|A\rangle$ ) basis, and  $|D\rangle = (|H\rangle + |V\rangle)/\sqrt{2}$ ,  $|A\rangle = (|H\rangle - |V\rangle)/\sqrt{2}$ . Taking the eighth frequency pair (194.292–192.708 THz) as an example, the interference curve of visibility as a function of phase  $\theta$  is shown in Fig. 2(a). The visibility is obtained from the coincidence counts measured by the four photon detectors, expressed as

$$V = \frac{(CC(DD) + CC(AA)) - (CC(DA) + CC(AD))}{CC(DD) + CC(AA) + CC(DA) + CC(AD)}, \quad (2)$$

where  $CC(DD)$ ,  $CC(DA)$ ,  $CC(AD)$ , and  $CC(AA)$  is the coincidence counts in the  $|D\rangle/|D\rangle$ ,  $|D\rangle/|A\rangle$ ,  $|A\rangle/|D\rangle$ , and  $|A\rangle/|A\rangle$  bases, respectively. In our experiment, we optimize the angle of the HWP so that the phase between  $H$  and  $V$  is  $\theta = 0$  and the ideal quantum state satisfies  $|\psi\rangle \propto (|HH\rangle + |VV\rangle)$ . With the temperature and the microheater-based feedback controls, this polarization state can be stably maintained over long time, as shown in Fig. 2(b).

We then perform QST of the polarization DOF for all frequency correlated pairs in the bases of  $|H\rangle/|V\rangle$ ,  $|D\rangle/|A\rangle$ , and  $|R\rangle/|L\rangle$ , where  $|R\rangle = (|H\rangle + i|V\rangle)/\sqrt{2}$ ,  $|L\rangle = (|H\rangle - i|V\rangle)/\sqrt{2}$ . Note that each PMA is equipped with two detectors, and the mutually orthogonal bases can be measured simultaneously. For example, all four basis states,  $|HH\rangle$ ,  $|HV\rangle$ ,  $|VH\rangle$ , and  $|VV\rangle$ , can be obtained in a single measurement. The fidelity to the  $|\Psi^+\rangle = \frac{1}{\sqrt{2}}(|HH\rangle + |VV\rangle)$  Bell state is estimated by coincidence

measurements in nine different measurement settings. Figure 2(c) shows an example of the reconstructed density matrices for the eighth frequency pair (194.292–192.708 THz). For all 22 frequency pairs, Fig. 2(d) shows that the observed fidelities are above 81.5% over a spectral range of 4.356 THz, among which there are 17 pairs of frequency channels with fidelities higher than 90%. The fidelity of the first frequency pair is lower than the others, probably because of its proximity to the pump. Fidelity decreases as the channel is farther away from the pump (still above 84.5%). This may be due to mechanisms such as limited SFWM bandwidth, unavoidable noise, etc., which we analyze further in Sec. IV. After subtracting the accidental coincidences, all net fidelities are above 94%. As shown in Fig. 2(e), when the pump power increases, the fidelity decreases due to multiphoton emission events in SFWM [50].

#### IV. PHOTONIC NOISE ANALYSIS AND QFC SOURCE CHARACTERIZATION

When pumped by the laser, photons can be generated not only by the SFWM process, i.e., generating correlated photon pairs, but also by linear processes, generating unwanted photonic noise. To characterize the single-photon spectrum and to identify the origins of noise, we program the WSS as a tunable band-pass filter operating from 191.289 to 196.239 THz with a step size of 33 GHz and a bandwidth of 20 GHz.

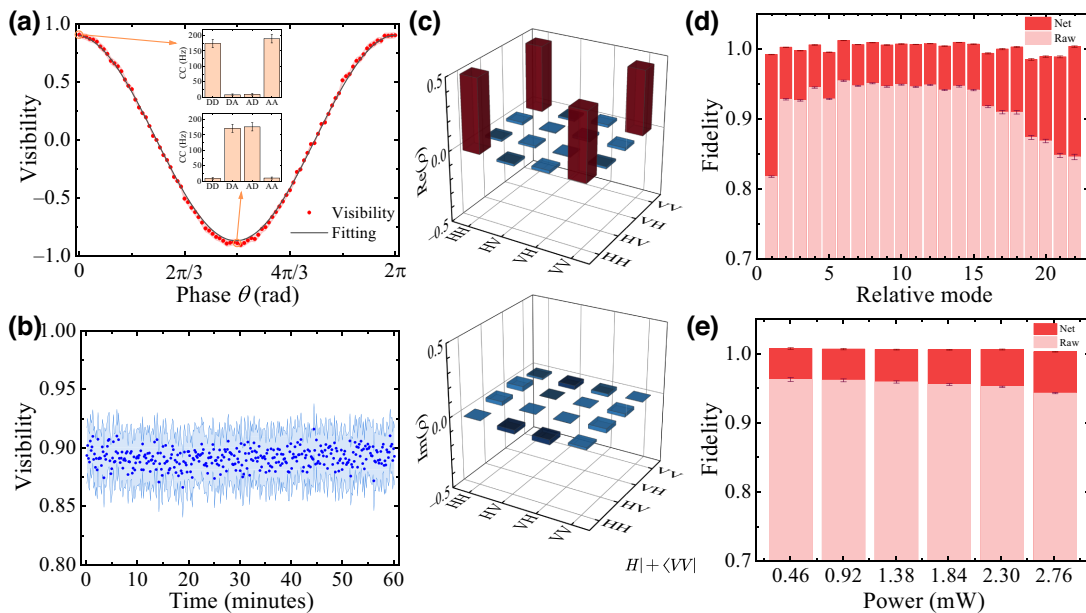


FIG. 2. (a) Visibility in the  $|D\rangle/|A\rangle$  basis as a function of the phase  $\theta$ . The insets show the two-photon coincidence counts for  $\theta = 0$  and  $\theta = \pi$  in the DA basis, respectively. (b) Visibility stability at  $\theta = 0$ . The shading in (a) and (b) represents the uncertainty in visibilities derived from Poisson statistics. (c) The real and imaginary part of the reconstructed density matrices  $\rho$  for the eighth frequency pair (194.292–192.708 THz). (d) Fidelities of the polarization entangled states for all 22 pairs. (e) Fidelity as a function of the pump power for the eighth frequency pair. The uncertainties of the fidelities in (d),(e) are derived from Poissonian statistics.

Figure 3(a) demonstrates the measured single-photon spectrum, which reveals a clear difference in the single counts between the on-resonance and off-resonance cases. The inset shows the single counts as a function of pump power at a frequency channel of 193.104 Hz (on resonance), and the data are fitted using the form  $aP^2 + bP + c$ , where the quadratic contribution  $aP^2$  comes from the photons generated by the SFWM, the linear contribution  $bP$  comes from the photonic noise generated by the spontaneous Raman scattering [30,51], and the constant term  $c$  comes from the dark count (include the noise generated by WSS). We get  $a = 3.90 \times 10^3 \text{ s}^{-1} \text{ mW}^{-2}$  for the quadratic term and  $b = 8.12 \times 10^3 \text{ s}^{-1} \text{ mW}^{-1}$  for the linear term in this comb line. In comparison, the linear fit to a nearby frequency channel (193.137 THz, off-resonance) shows an off-resonance linear term of  $7.73 \times 10^2 \text{ s}^{-1} \text{ mW}^{-1}$ . In Fig. 3(b), all frequency channels are analyzed and the linear and quadratic terms are extracted. For the 101 off-resonance frequency channels, we obtain an average linear term coefficient of  $1.22 \times 10^3 \text{ s}^{-1} \text{ mW}^{-1}$ , while for the on-resonance frequency channels (except the pump channel) it increases to  $1.01 \times 10^4 \text{ s}^{-1} \text{ mW}^{-1}$ . That is, the

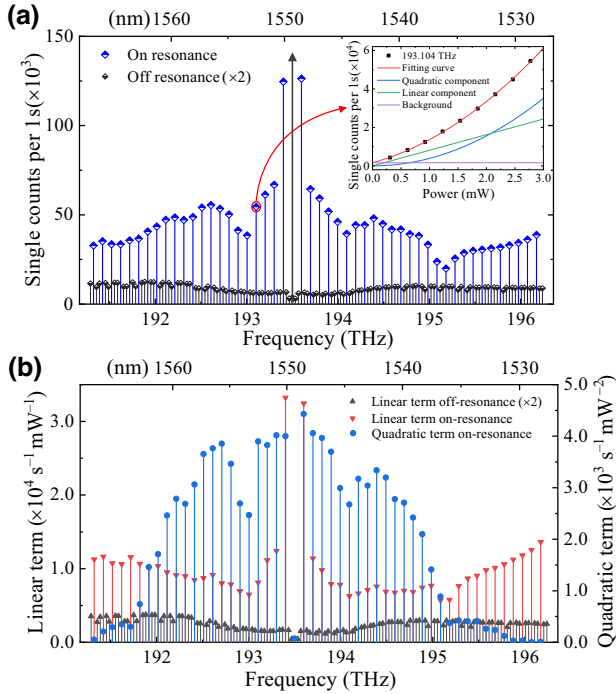


FIG. 3. (a) Single-photon spectrum of the MRR for both on- and off-resonance cases. The minimum frequency separation is 33 GHz for different channels and there are two off-resonance lines between every two adjacent resonance lines. The inset shows the single counts of a comb line (channel centered at 193.104 Hz) as a function of the pump power level. (b) The linear and quadratic terms can be separated and used to analyze photon noise by fitting each frequency line. The values for the nonresonant cases are multiplied by 2 in (a),(b).

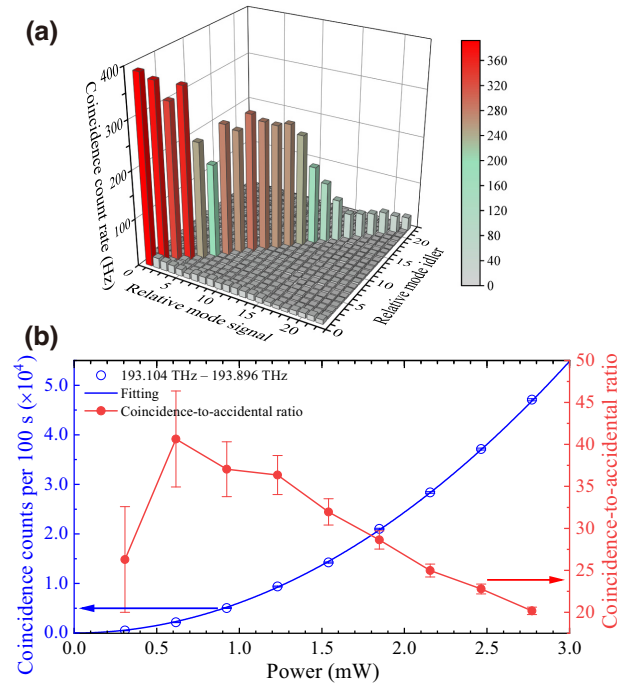


FIG. 4. (a) Joint spectral intensity for 22 accessible signal-idler pairs. (b) Coincidence counts and the calculated coincidence-to-accidental ratio (CAR) versus the pump power. Error bars are derived from Poissonian statistics.

photonic noise generated outside the ring is much smaller than that at on resonance, proving that there is additional photonic noise generated inside the MRR [24,25]. We also found that the average value of the linear term in the low-frequency part of the nonresonant channel is  $1.32 \times 10^3 \text{ s}^{-1} \text{ mW}^{-1}$ , which is slightly higher than that in the high-frequency part with an average value of  $1.14 \times 10^3 \text{ s}^{-1} \text{ mW}^{-1}$ , indicating the asymmetry of the noise spectrum, i.e., the Stokes part is larger than the anti-Stokes part [51]. For the quadratic term in the on-resonance case, we found that only 16 pairs of frequency channels in a range of 3.168 THz are highly efficient for generating correlated photon pairs, while the other channels are dominated by photonic noise, revealing a photon-pair generation bandwidth of approximately 25.4 nm due to anomalous group-delay dispersion (GVD) at the excitation wavelength [52].

Satisfying the energy conservation, the photon pairs generated by the SFWM process are spectrally symmetrically distributed on both sides of the pump, which is a multiwavelength two-photon entanglement source. To observe the frequency correlations over a wide spectral range, we characterized the joint spectral intensity (JSI) between combinations of frequency modes spanning a  $22 \times 22$  Hilbert space [28]. The JSI with channel bandwidth of 20 GHz and channel spacing of 99 GHz is shown in Fig. 4(a). As expected, there is a strong correlation

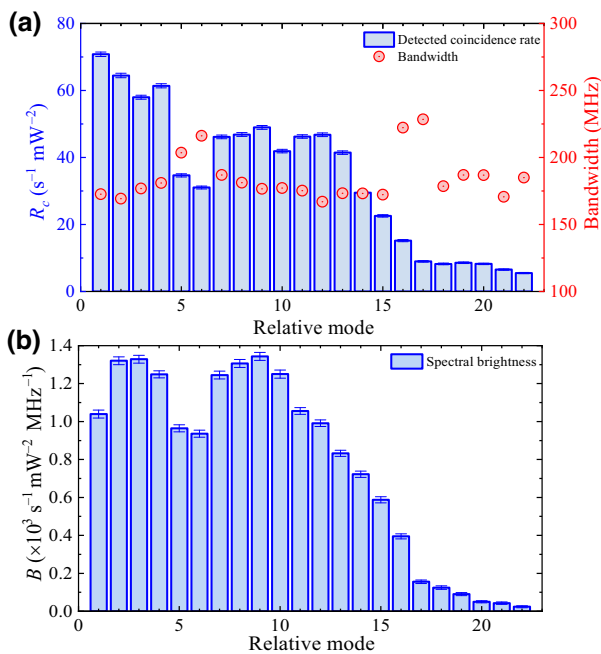


FIG. 5. (a) Detected net coincidence rate  $R_c$  and bandwidth for the respective frequency pairs. The bandwidth is derived from the temporal correlation histogram, and agrees with classical characterization results. (b) Spectral brightness  $B$  for all 22 pairs. Error bars are derived from Poissonian statistics.

between the frequency-symmetric comb lines on the diagonal, reflecting the energy conservation during the SFWM process. We also noticed that the coincidence counts of the 17th to 22nd channel pairs are relatively low, which is consistent with the relative low quadratic term shown in Fig. 3(b). For frequency-correlated photon pairs, the coincidence counts (CC) and the coincidence-to-accidental ratio (CAR) are measured. Taking a particular frequency pair (193.104–193.896 THz) shown in Fig. 4(b) as an example, the maximum CAR achievable is 41, which can be improved by reducing signal and idler photon losses. For the 22 pairs of correlated channels on the diagonal, we measured the coincidence counts at different pump-power levels, and derived the detected net coincidence rate  $R_c$  with the unit of  $s^{-1} mW^{-2}$ . The results are shown in Fig. 5(a). Following the method described in Ref. [18], we obtained an average bandwidth of 184.58 MHz for each pair, which is in good agreement with the linewidth of the MRR. Figure 5(b) shows the spectral brightness  $B$  with a unit of  $s^{-1} mW^{-2} MHz^{-1}$ , which is independent of collection efficiency. Refer to Appendix E for the detailed definition of the detected net coincidence rate  $R_c$  and the spectral brightness  $B$ .

The collection efficiency [53,54] of the signal (idler) channel shown in Fig. 6(a) can be obtained by dividing the biphoton coincidence count rate  $R_c$  by the single-photon count rate  $R_i$  ( $R_s$ ) of the idler (signal) channel, which contains the ring-to-bus extraction efficiency, the

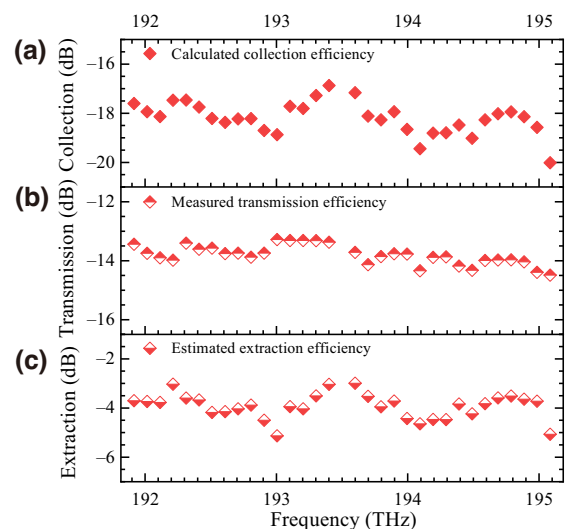


FIG. 6. (a) The calculated collection efficiency, (b) the measured transmission efficiency (include the fiber-to-chip coupling efficiency), and (c) the estimated ring-to-bus extraction efficiency for different frequency channels.

total transmission efficiency [include the fiber-to-chip coupling efficiency (approximately 50%)] and the detection efficiency (approximately 90%). For the 16 generated frequency pairs, we measured the transmission losses of the signal and idler channels, as shown in Fig. 6(b). Subtracting the total transmission loss and detection loss from the collection efficiency gives us the ring-to-bus waveguide extraction efficiency shown in Fig. 6(c), with an average value of 40.79% ( $-3.92$  dB). Further optimization of the coupling conditions to slightly overcoupling can improve the extraction efficiency and also the photon-pair generation rate [24].

The source brightness decays rapidly due to the limited SFWM bandwidth, which is consistent with the results shown in Fig. 3(b). And the single counts becoming increasingly dominated by noise as the frequency pair moves away from the pump. Meanwhile, the first frequency channel pair, which is closest to the pump, is affected by the noise photons, reducing its quality. Although the observed fidelity is greater than 81% for all channel pairs, we recognize that further research is needed to increase the number and quality of channel pairs. For the SFWM bandwidth, the GVD in waveguide can be tailored to achieve anomalous GVD over a broader bandwidth [55]. The effect of higher pump power level on the bandwidth also needs to be investigated. Increasing the number of channel pairs can also be achieved by increasing the cavity length of the microresonator, i.e., reducing the FSR, for a fixed bandwidth. With advances in integrated photonics, the entire platform can be integrated on a monolithic chip, reducing losses. Cryogenic cooling of the chip can suppress the photon noise generated in the chip [20,56]. All the

above-mentioned points could improve the signal-to-noise ratio, and enables higher-quality quantum light sources.

## V. DISCUSSION AND CONCLUSION

In contrast to the generation of photon pairs in nonlinear bulk crystals or waveguides with subsequent narrow-band spectral filtering, microresonators with multiple frequency nature can efficiently generate discrete, equally spaced frequency combs. The extensibility of the frequency modes of QFC, with the additional entanglement of other DOF, allows the generation of frequency-multiplexed heralded photons and multiphoton, high-dimensional, and hyperentangled states [57,58]. Meanwhile, the polarization entanglement source uses the well-established PAM for entanglement analysis, eliminating the requirement for the phase stability of the interferometer in the energy-time entanglement analyzers. And the use of higher  $Q$ -factor microresonators can lead to narrower photon bandwidth and higher photon-pair generation rates, resulting in higher spectral brightness, which may bring quantum light sources into real-world application scenarios.

The rapid development of integrated photonics [59–61] in recent years has made it possible to realize higher  $Q$ -factor microresonators. Meanwhile, integrated photonic devices, such as polarization beam splitter and polarization rotator [62,63], have been rapidly developed, which provides a promising solution for fully integrated, compact, stable, and scalable polarization entanglement sources. We also noticed that the SFWM bandwidth of our MRR is approximately 3 THz, which may attribute to the relatively low pump power level and the nonoptimal dispersion engineering of the waveguide. Cryogenic cooling, better dispersion engineering, smaller FSR (narrower frequency-mode spacing), can provide more frequency modes with efficient pair generation rate, which is very helpful for realizing large-scale QNs based on WDM.

In summary, we have demonstrated a polarization-entangled biphoton QFC by placing an integrated silicon-nitride MRR within a Sagnac interferometer. We show that our MRR-based Sagnac-configured source can simultaneously generate 22 parallel frequency pairs in a range of approximately 4 THz. Using quantum state tomography to quantify the entanglement of each channel pair, the observed fidelity exceeds 81% in all frequency ranges. The freedom of the Sagnac interferometer from phase control between different paths, together with the feedback control we developed based on hysteretic behavior, allows our source to be highly stable against external perturbations. In addition, the presented setup has the potential to be integrated into a single chip, which can further improve the stability of the system. Our research provides a scalable and integrated platform for the generation of various entangled photonic states, as well as for the experimental

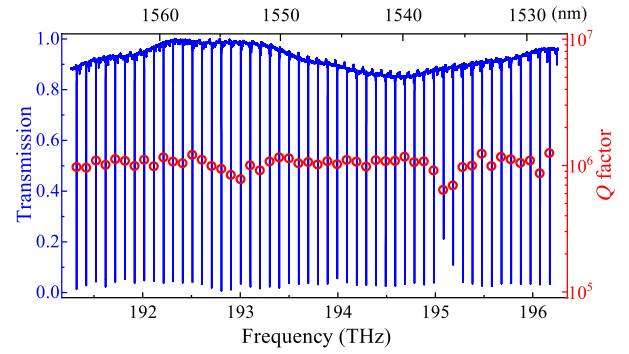


FIG. 7. Transmission spectrum and  $Q$  factors for 50 resonances from 191.269 to 196.259 THz, with a free spectral range of approximately 99 GHz.

realization of high-dimensional quantum computing and large-scale QNs.

## ACKNOWLEDGMENTS

This research was supported by the National Key Research and Development Program of China (Grants No. 2022YFE0137000, No. 2019YFA0308704), the Leading-Edge Technology Program of Jiangsu Natural Science Foundation (Grant No. BK20192001), the Fundamental Research Funds for the Central Universities, the Innovation Program for Quantum Science and Technology (Grants No. 2021ZD0300700 and No. 2021ZD0301500), and the program B for Outstanding PhD candidate of Nanjing University.

## APPENDIX A: CAVITY RESONANCES

The transmission spectrum of the MRR around the telecom C-band is measured using a tunable laser (Santec TSL-570) under near-cold cavity conditions, and a total of 50 resonances were obtained from 191.269 to 196.259 THz, as shown in Fig. 7. We derived quality factors for all measured resonances, which exhibited an average FWHM of 190.41 MHz and an average  $Q$  factor of  $1.03 \times 10^6$ . An experimental value for the free spectral range (FSR) of 99.03 GHz is obtained by averaging the frequency spacings of adjacent resonances.

## APPENDIX B: THERMAL CONTROL OF THE RESONANCES

For the thermal control of the resonance of the MRR, we have designed an integrated microheater placed at the top of the ring waveguide, which has an electrical resistance of about 2050  $\Omega$ . Due to the thermo-optical effect, electrically driving the integrated heater changes the refractive index of the waveguide, thereby adjusting the spectral positions of the cavity resonances. The chip is mounted on a copper

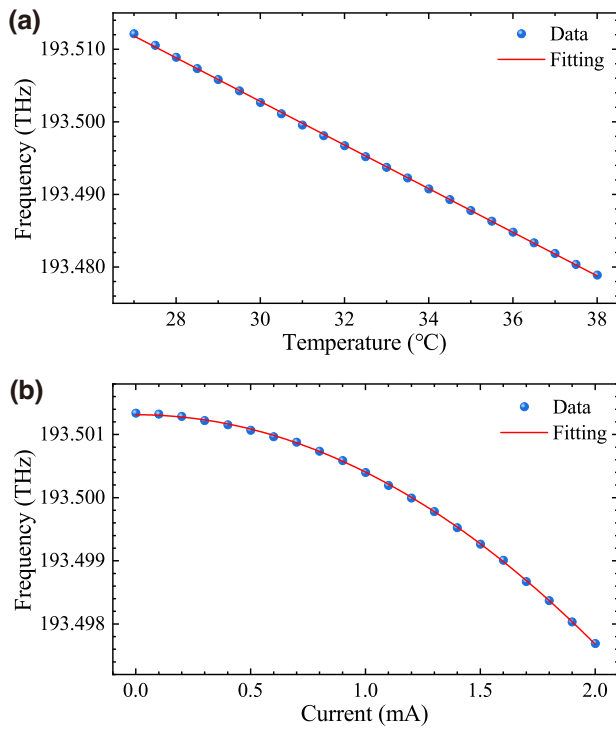


FIG. 8. Resonant frequency of the MRR as a function of (a) chip temperature, (b) current applied to the integrated microheater.

plate with a thermoelectric cooler (TEC) and a negative temperature coefficient (NTC) thermistor connected to a high-performance digital temperature controller (Thorlabs TED4015) to stabilize the temperature ( $<0.001$  °C) of the entire chip. When the pump power is relatively low (i.e., near a cold cavity), the cavity resonance exhibits a Lorentzian lineshape. And we find a resonance shift of about  $-3.01$  GHz/°C for the temperature tuning and about  $-0.91$  GHz/mA<sup>2</sup> or  $-0.44$  GHz/mW for the current tuning, according to Fig. 8.

### APPENDIX C: THE HYSTERETIC BEHAVIOR

Figure 9 shows the hysteresis behavior for different pump levels, where the pump frequency is fixed at 193.5 THz and the microheater current is tuned so that the cavity resonance sweeps across the pump line. Note that the cavity Lorentz is initially to the left of the pump line. A forward current sweep (increase in current) is equivalent to a backward wavelength sweep (decrease in pump wavelength) and vice versa. As the current decreases (corresponding to the pump wavelength approaching the cavity resonance from the left), the heat flowing into the cavity increases and the cavity begins to heat up, drifting the cavity resonance away from the cold-cavity resonance wavelength. The rise of cavity temperature stops when the absorption is maximal and cannot be further compensated by the heater dissipation. The cavity resonance cannot

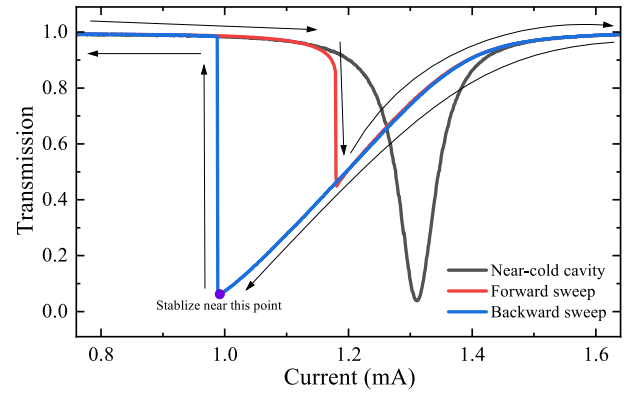


FIG. 9. Hysteresis behavior of the pump resonance with the laser frequency fixed at 193.5 THz. The cavity resonance exhibits a Lorentzian lineshape under near-cold cavity condition (0.015 mW). The current of the microheater is tuned forward and backward with a pump power of 2.773 mW.

be pushed any further and the pump power in the cavity drops quickly. However, as the current increases, the pump approaches the cavity resonance from the right side, and the upward shift of the cavity resonance is accelerated as the cavity heats up. The scan rate across the cavity lineshape is sufficiently fast and prevents the resonator from fully “charging,” resulting in the measured transmission not reaching the minimum.

### APPENDIX D: LONG-TERM STABLE OPERATION OF THE SOURCE

Stable pumping of a high- $Q$  microresonator with narrow linewidth needs to overcome environmental perturbations caused by temperature, wavelength, power, etc. And the existence of hysteresis behavior makes it easier for the microresonator to drop out of resonance. Whereas, the broadening of the cavity lineshape provides a larger range to stabilize the cavity near the resonance point (i.e., the minimum transmission point) of the pump. We monitor the pump power after the postfilter, then decrease the current to push the cavity resonance toward the pump line and stay just before the minimum transmission point. If there is a small decrease in pump transmission, it means that the heat flowing into the cavity is increasing, we can increase the current to push the cavity resonance away from the pump to cool the cavity. Similarly, the current should decrease when an increase in transmittance is detected. As shown in Fig. 10, this feedback control of the cavity resonances, combined with the temperature control of the chip, allows us to stabilize the cavity near the resonance with a transmission of 0.05, corresponding to an extinction ratio of approximately 13 dB.



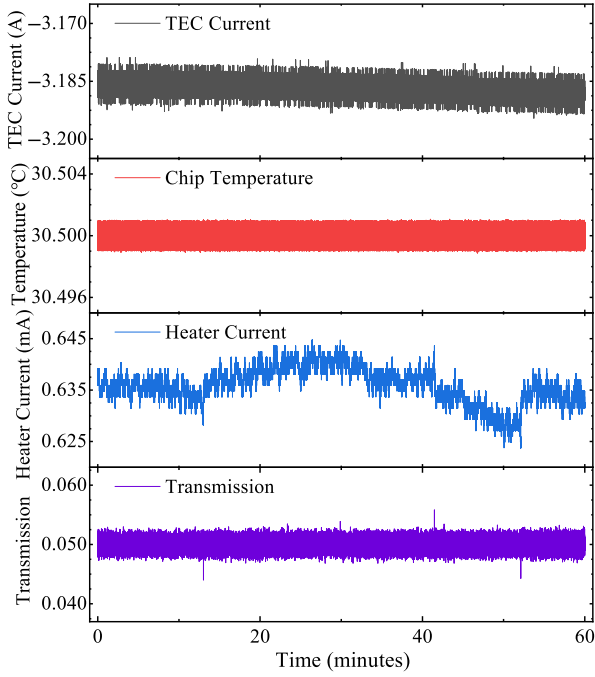


FIG. 10. Resonance stability with the help of chip temperature control and microheater-based feedback control.

### APPENDIX E: SPECTRAL BRIGHTNESS AND COLLECTION EFFICIENCY

In our experiment, the number of signal and idler photons detected by SNSPDs per second ( $N_s$  and  $N_i$ ) are not only generated by the SFWM process, but also by the spontaneous Raman scattering [51] and the dark counts ( $N_{DC,s}$  and  $N_{DC,i}$ ), and the subscripts  $s$  and  $i$  represent signal and idler, respectively. Taking into account the intrinsic photon-pair generation rate ( $R_{PGR}$ ) and the collection efficiency of each channel ( $\eta_s$  and  $\eta_i$ ), these parameters are related to each other through the following formulas [53,64]:

$$\begin{aligned}
 N_s &= \eta_s \times R_{PGR} \times P^2 + R_{RS,s} \times P + N_{DC,s} \\
 &= R_s \times P^2 + R_{RS,s} \times P + N_{DC,s}, \\
 N_i &= \eta_i \times R_{PGR} \times P^2 + R_{RS,i} \times P + N_{DC,i} \\
 &= R_i \times P^2 + R_{RS,i} \times P + N_{DC,i},
 \end{aligned} \tag{E1}$$

where  $P$  is the input power of pump, the collection efficiencies  $\eta_s$  and  $\eta_i$  contains the ring-to-bus waveguide extraction efficiency, the total transmission efficiency [include the fiber-to-chip coupling efficiency (approximately 50%)] and the detection efficiency (approximately 90%), the quadratic coefficient  $R_{s(i)} = \eta_{s(i)} \times R_{PGR}$  here is the detected single-photon count rate associated with SFWM in the unit of  $s^{-1} \text{ mW}^{-2}$ . The linear coefficient  $R_{RS,s(i)}$  is the noise term that associated with Raman scattering, which includes the contributions of the input and

output fiber, the silicon-nitride bus waveguide and the microring. For the nonresonant case, the quadratic term is close to zero, and there is almost no contribution of the microring to the noise in the linear coefficient. Meanwhile, the detected coincidence counts per second of the photon pairs satisfy

$$\begin{aligned}
 N_c &= \eta_s \times \eta_i \times R_{PGR} \times P^2 + N_{AC} \\
 &= R_c \times P^2 + N_{AC},
 \end{aligned} \tag{E2}$$

where  $N_{AC}$  is the accidental coincidence count rate in the coincidence window, and the quadratic coefficient  $R_c = \eta_s \times \eta_i \times R_{PGR}$  is the detected net coincidence rate in the unit of  $s^{-1} \text{ mW}^{-2}$ , which includes the losses experienced by signal and idler photons. Thus, the intrinsic pair generation rate, which excludes all losses, can be calculated by the following formula:

$$R_{PGR} = \frac{R_s \times R_i}{R_c} (s^{-1} \text{ mW}^{-2}). \tag{E3}$$

Spectral brightness  $B$  is defined as the number of photon pairs generated by a light source per second per unit pump power per megahertz of bandwidth, and can be calculated by dividing the  $R_{PGR}$  by the corresponding bandwidth with a unit of  $s^{-1} \text{ mW}^{-2} \text{ MHz}^{-1}$ . The loss on the signal and idler photons, that is, the collection efficiency, can be derived by

$$\eta_s = \frac{R_c}{R_s} \quad \text{and} \quad \eta_i = \frac{R_c}{R_i}. \tag{E4}$$

The ring-to-bus waveguide coupling loss can then be estimated by subtracting the experimentally measured total transmission loss and detection loss from the collection loss.

### APPENDIX F: THE SANDWICHED QWP-HWP-QWP SETUP

In the sandwiched “QWP-HWP-QWP” waveplate combination, the angle of the two QHP is fixed at  $45^\circ$ , and the angle of the middle half-wave plate is marked as  $\phi$ . Then the Jones matrix after the input state  $[1; e^{i\theta}]$  passes through “QWP-HWP-QWP” can be expressed as

$$\begin{aligned}
 \mathbf{J}_{\text{output}} &= \mathbf{J}_{\text{QWP}}\left(\frac{\pi}{4}\right) \cdot \mathbf{J}_{\text{HWP}}(\phi) \cdot \mathbf{J}_{\text{QWP}}\left(\frac{\pi}{4}\right) \cdot \begin{pmatrix} 1 \\ e^{i\theta} \end{pmatrix} \\
 &= \begin{pmatrix} e^{i(\frac{\pi}{2}-2\phi)} & 0 \\ 0 & e^{i(2\phi-\frac{\pi}{2})} \end{pmatrix} \begin{pmatrix} 1 \\ e^{i\theta} \end{pmatrix} \\
 &= \begin{pmatrix} e^{i(\frac{\pi}{2}-2\phi)} \\ e^{i(2\phi-\frac{\pi}{2}+\theta)} \end{pmatrix} \\
 &= e^{i(\frac{\pi}{2}-2\phi)} \begin{pmatrix} 1 \\ e^{i(4\phi+\theta-\pi)} \end{pmatrix}.
 \end{aligned} \tag{F1}$$

In order to compensate for the relative phase difference  $\theta$  between  $|HH\rangle$  and  $|VV\rangle$ , the phase  $\theta$  and the angle of the HWP  $\varphi$  need to satisfy

$$4\phi + \theta = \pi. \quad (\text{F2})$$

That is, the phase difference  $\theta$  between  $|HH\rangle$  and  $|VV\rangle$  to be compensated is 4 times the angle of the HWP  $\varphi$  (plus an additional constant).

- 
- [1] J. F. Clauser and A. Shimony, Bell's theorem. experimental tests and implications, *Rep. Prog. Phys.* **41**, 1881 (1978).
- [2] A. Aspect, P. Grangier, and G. Roger, Experimental realization of Einstein-Podolsky-Rosen-Bohm Gedanken experiment: A new violation of Bell's inequalities, *Phys. Rev. Lett.* **49**, 91 (1982).
- [3] D. M. Greenberger, M. A. Horne, A. Shimony, and A. Zeilinger, Bell's theorem without inequalities, *Am. J. Phys.* **58**, 1131 (1990).
- [4] B. Hensen, H. Bernien, A. E. Dréau, A. Reiserer, N. Kalb, M. S. Blok, J. Ruitenber, R. F. L. Vermeulen, R. N. Schouten, C. Abellán, W. Amaya, V. Pruneri, M. W. Mitchell, M. Markham, D. J. Twitchen, D. Elkouss, S. Wehner, T. H. Tamini, and R. Hanson, Loophole-free Bell inequality violation using electron spins separated by 1.3 kilometres, *Nature* **526**, 682 (2015).
- [5] M. Giustina, *et al.*, Significant-loophole-free test of Bell's theorem with entangled photons, *Phys. Rev. Lett.* **115**, 250401 (2015).
- [6] L. K. Shalm, *et al.*, Strong loophole-free test of local realism, *Phys. Rev. Lett.* **115**, 250402 (2015).
- [7] W. Rosenfeld, D. Burchardt, R. Garthoff, K. Redeker, N. Ortegel, M. Rau, and H. Weinfurter, Event-ready Bell test using entangled atoms simultaneously closing detection and locality loopholes, *Phys. Rev. Lett.* **119**, 010402 (2017).
- [8] R. Ursin, F. Tiefenbacher, T. Schmitt-Manderbach, H. Weier, T. Scheidl, M. Lindenthal, B. Blauensteiner, T. Jennewein, J. Perdigues, P. Trojek, B. Ömer, M. Fürst, M. Meyenburg, J. Rarity, Z. Sodnik, C. Barbieri, H. Weinfurter, and A. Zeilinger, Entanglement-based quantum communication over 144 km, *Nat. Phys.* **3**, 481 (2007).
- [9] A. Fedrizzi, R. Ursin, T. Herbst, M. Nespola, R. Prevedel, T. Scheidl, F. Tiefenbacher, T. Jennewein, and A. Zeilinger, High-fidelity transmission of entanglement over a high-loss free-space channel, *Nat. Phys.* **5**, 389 (2009).
- [10] J. Yin, *et al.*, Satellite-based entanglement distribution over 1200 kilometers, *Science* **356**, 1140 (2017).
- [11] J. Yin, *et al.*, Satellite-to-ground entanglement-based quantum key distribution, *Phys. Rev. Lett.* **119**, 200501 (2017).
- [12] J.-G. Ren, *et al.*, Ground-to-satellite quantum teleportation, *Nature* **549**, 70 (2017).
- [13] Z. Xie, T. Zhong, S. Shrestha, X. Xu, J. Liang, Y.-X. Gong, J. C. Bienfang, A. Restelli, J. H. Shapiro, F. N. C. Wong, and C. W. Wong, Harnessing high-dimensional hyperentanglement through a biphoton frequency comb, *Nat. Photonics* **9**, 536 (2015).
- [14] C. Joshi, A. Farsi, S. Clemmen, S. Ramelow, and A. L. Gaeta, Frequency multiplexing for quasi-deterministic heralded single-photon sources, *Nat. Commun.* **9**, 847 (2018).
- [15] S. Wengerowsky, S. K. Joshi, F. Steinlechner, H. Hübel, and R. Ursin, An entanglement-based wavelength-multiplexed quantum communication network, *Nature* **564**, 225 (2018).
- [16] S. K. Joshi, D. Aktas, S. Wengerowsky, M. Lončarić, S. P. Neumann, B. Liu, T. Scheidl, G. C. Lorenzo, Željko Samec, L. Kling, A. Qiu, M. Razavi, M. Stipčević, J. G. Rarity, and R. Ursin, A trusted node-free eight-user metropolitan quantum communication network, *Sci. Adv.* **6**, eaba0959 (2020).
- [17] X. Liu, J. Liu, R. Xue, H. Wang, H. Li, X. Feng, F. Liu, K. Cui, Z. Wang, L. You, Y. Huang, and W. Zhang, 40-user fully connected entanglement-based quantum key distribution network without trusted node, *PhotonIX* **3**, 1 (2022).
- [18] W. Wen, Z. Chen, L. Lu, W. Yan, W. Xue, P. Zhang, Y. Lu, S. Zhu, and X. S. Ma, Realizing an entanglement-based multiuser quantum network with integrated photonics, *Phys. Rev. Appl.* **18**, 024059 (2022).
- [19] L. Chang, S. Liu, and J. E. Bowers, Integrated optical frequency comb technologies, *Nat. Photonics* **16**, 95 (2022).
- [20] X. Li, P. L. Voss, J. E. Sharping, and P. Kumar, Optical-fiber source of polarization-entangled photons in the 1550 nm telecom band, *Phys. Rev. Lett.* **94**, 053601 (2005).
- [21] L. G. Helt, Z. Yang, M. Liscidini, and J. E. Sipe, Spontaneous four-wave mixing in microring resonators, *Opt. Lett.* **35**, 3006 (2010).
- [22] F. Mazeas, M. Traetta, M. Bentivegna, F. Kaiser, D. Aktas, W. Zhang, C. A. Ramos, L. A. Ngah, T. Lunghi, E. Picholle, N. Belabas-Plougonven, X. L. Roux, E. Casan, D. Marris-Morini, L. Vivien, G. Sauder, L. Labonté, and S. Tanzilli, High-quality photonic entanglement for wavelength-multiplexed quantum communication based on a silicon chip, *Opt. Express* **24**, 28731 (2016).
- [23] J. A. Jaramillo-Villegas, P. Imany, O. D. Odele, D. E. Leaird, Z.-Y. Ou, M. Qi, and A. M. Weiner, Persistent energy-time entanglement covering multiple resonances of an on-chip biphoton frequency comb, *Optica* **4**, 655 (2017).
- [24] Y.-R. Fan, C. Lyu, C.-Z. Yuan, G.-W. Deng, Z.-Y. Zhou, Y. Geng, H.-Z. Song, Y. Wang, Y.-F. Zhang, R.-B. Jin, H. Zhou, L.-X. You, Z. Wang, G.-C. Guo, and Q. Zhou, Multi-wavelength quantum light sources on silicon nitride microring chip, *Laser Photonics Rev.* **17**, 2300172 (2023).
- [25] F. Samara, A. Martin, C. Autebert, M. Karpov, T. J. Kippenberg, H. Zbinden, and R. Thew, High-rate photon pairs and sequential time-bin entanglement with Si<sub>3</sub>N<sub>4</sub> microring resonators, *Opt. Express* **27**, 19309 (2019).
- [26] F. Samara, N. Maring, A. Martin, A. S. Raja, T. J. Kippenberg, H. Zbinden, and R. Thew, Entanglement swapping between independent and asynchronous integrated photon-pair sources, *Quantum Sci. Technol.* **6**, 045024 (2021).
- [27] J. Chen, Z. H. Levine, J. Fan, and A. L. Migdall, Frequency-bin entangled comb of photon pairs from a silicon-on-insulator micro-resonator, *Opt. Express* **19**, 1470 (2011).
- [28] P. Imany, J. A. Jaramillo-Villegas, O. D. Odele, K. Han, D. E. Leaird, J. M. Lukens, P. Lougovski, M. Qi, and A. M. Weiner, 50-GHz-spaced comb of high-dimensional frequency-bin entangled photons from an on-chip silicon nitride microresonator, *Opt. Express* **26**, 1825 (2018).

- [29] C. Reimer, L. Caspani, M. Clerici, M. Ferrera, M. Kues, M. Peccianti, A. Pasquazi, L. Razzari, B. E. Little, S. T. Chu, D. J. Moss, and R. Morandotti, Integrated frequency comb source of heralded single photons, *Opt. Express* **22**, 6535 (2014).
- [30] C. Reimer, M. Kues, P. Roztocky, B. Wetzels, F. Grazioso, B. E. Little, S. T. Chu, T. Johnston, Y. Bromberg, L. Caspani, D. J. Moss, and R. Morandotti, Generation of multiphoton entangled quantum states by means of integrated frequency combs, *Science* **351**, 1176 (2016).
- [31] M. Kues, C. Reimer, J. M. Lukens, W. J. Munro, A. M. Weiner, D. J. Moss, and R. Morandotti, Quantum optical microcombs, *Nat. Photonics* **13**, 170 (2019).
- [32] K. Guo, X. Shi, X. Wang, J. Yang, Y. Ding, H. Ou, and Y. Zhao, Generation rate scaling: The quality factor optimization of microring resonators for photon-pair sources, *Photonics Res.* **6**, 587 (2018).
- [33] D. Lago-Rivera, S. Grandi, J. V. Rakonjac, A. Seri, and H. de Riedmatten, Telecom-heralded entanglement between multimode solid-state quantum memories, *Nature* **594**, 37 (2021).
- [34] A. Poppe, A. Fedrizzi, R. Ursin, H. R. Böhm, T. Lorünser, O. Maurhardt, M. Peev, M. Suda, C. Kurtsiefer, H. Weinfurter, T. Jennewein, and A. Zeilinger, Practical quantum key distribution with polarization entangled photons, *Opt. Express* **12**, 3865 (2004).
- [35] Z. Tang, Z. Liao, F. Xu, B. Qi, L. Qian, and H.-K. Lo, Experimental demonstration of polarization encoding measurement-device-independent quantum key distribution, *Phys. Rev. Lett.* **112**, 190503 (2014).
- [36] T. Kim, M. Fiorentino, and F. N. C. Wong, Phase-stable source of polarization-entangled photons using a polarization sagnac interferometer, *Phys. Rev. A* **73**, 012316 (2006).
- [37] A. Fedrizzi, T. Herbst, A. Poppe, T. Jennewein, and A. Zeilinger, A wavelength-tunable fiber-coupled source of narrowband entangled photons, *Opt. Express* **15**, 15377 (2007).
- [38] S. Wengerowsky, S. K. Joshi, F. Steinlechner, J. R. Zichi, S. M. Dobrovolskiy, R. van der Molen, J. W. N. Los, V. Zwiller, M. A. M. Versteegh, A. Mura, D. Calonico, M. Inguscio, H. Hübel, L. Bo, T. Scheidl, A. Zeilinger, A. Xuereb, and R. Ursin, Entanglement distribution over a 96-km-long submarine optical fiber, *Proc. Natl. Acad. Sci.* **116**, 6684 (2019).
- [39] H.-Y. Liu, X.-H. Tian, C. Gu, P. Fan, X. Ni, R. Yang, J.-N. Zhang, M. Hu, J. Guo, X. Cao, X. Hu, G. Zhao, Y.-Q. Lu, Y.-X. Gong, Z. Xie, and S.-N. Zhu, Drone-based entanglement distribution towards mobile quantum networks, *Natl. Sci. Rev.* **7**, 921 (2020).
- [40] J. Yin, *et al.*, Entanglement-based secure quantum cryptography over 1120 kilometres, *Nature* **582**, 501 (2020).
- [41] T. van Leent, M. Bock, R. Garthoff, K. Redeker, W. Zhang, T. Bauer, W. Rosenfeld, C. Becher, and H. Weinfurter, Long-distance distribution of atom-photon entanglement at telecom wavelength, *Phys. Rev. Lett.* **124**, 010510 (2020).
- [42] S. P. Neumann, M. Selimovic, M. Bohmann, and R. Ursin, Experimental entanglement generation for quantum key distribution beyond 1 Gbit/s, *Quantum* **6**, 822 (2022).
- [43] T. Yamazaki, R. Ikuta, T. Kobayashi, S. Miki, F. China, H. Terai, N. Imoto, and T. Yamamoto, Massive-mode polarization entangled biphoton frequency comb, *Sci. Rep.* **12**, 8964 (2022).
- [44] M.-H. Jiang, W. Xue, Q. He, Y.-Y. An, X. Zheng, W.-J. Xu, W. Wen, Y.-B. Xie, Y. Lu, S. Zhu, and X.-S. Ma, Quantum storage of entangled photons at telecom wavelengths in a crystal, *ArXiv:2212.12898* (2022).
- [45] N. B. Lingaraju, H.-H. Lu, S. Seshadri, D. E. Leaird, A. M. Weiner, and J. M. Lukens, Adaptive bandwidth management for entanglement distribution in quantum networks, *Optica* **8**, 329 (2021).
- [46] M. Alshowkan, B. P. Williams, P. G. Evans, N. S. V. Rao, E. M. Simmerman, H.-H. Lu, N. B. Lingaraju, A. M. Weiner, C. E. Marvinney, Y.-Y. Pai, B. J. Lawrie, N. A. Peters, and J. M. Lukens, Reconfigurable quantum local area network over deployed fiber, *PRX Quantum* **2**, 040304 (2021).
- [47] H. Mahmudlu, R. Johanning, A. Van Rees, A. Khodadad Kashi, J. P. Epping, R. Haldar, K.-J. Boller, and M. Kues, Fully on-chip photonic turnkey quantum source for entangled qubit/qudit state generation, *Nat. Photonics* **17**, 518 (2023).
- [48] D. F. V. James, P. G. Kwiat, W. J. Munro, and A. G. White, Measurement of qubits, *Phys. Rev. A* **64**, 052312 (2001).
- [49] T. Carmon, L. Yang, and K. J. Vahala, Dynamical thermal behavior and thermal self-stability of microcavities, *Opt. Express* **12**, 4742 (2004).
- [50] Y. H. Li, Z. Y. Zhou, L. T. Feng, W. T. Fang, S. L. Liu, S. K. Liu, K. Wang, X. F. Ren, D. S. Ding, L. X. Xu, and B. S. Shi, On-chip multiplexed multiple entanglement sources in a single silicon nanowire, *Phys. Rev. Appl.* **7**, 064005 (2017).
- [51] Q. Lin, F. Yaman, and G. P. Agrawal, Photon-pair generation in optical fibers through four-wave mixing: Role of raman scattering and pump polarization, *Phys. Rev. A* **75**, 023803 (2007).
- [52] M. Zhang, L.-T. Feng, Z.-Y. Zhou, Y. Chen, H. Wu, M. Li, S.-M. Gao, G.-P. Guo, G.-C. Guo, D.-X. Dai, and X.-F. Ren, Generation of multiphoton quantum states on silicon, *Light-Sci. Appl.* **8**, 41 (2019).
- [53] E. Engin, D. Bonneau, C. M. Natarajan, A. S. Clark, M. G. Tanner, R. H. Hadfield, S. N. Dorenbos, V. Zwiller, K. Ohira, N. Suzuki, H. Yoshida, N. Iizuka, M. Ezaki, J. L. O'Brien, and M. G. Thompson, Photon pair generation in a silicon micro-ring resonator with reverse bias enhancement, *Opt. Express* **21**, 27826 (2013).
- [54] J. Li, C. Yuan, S. Shen, Z. Zhang, R. Zhang, H. Li, Y. Wang, G. Deng, L. You, Z. Wang, H. Song, Y. Fan, G. Guo, and Q. Zhou, Discrete frequency-bin entanglement generation via cascaded second-order nonlinear processes in Sagnac interferometer, *Opt. Lett.* **48**, 2917 (2023).
- [55] A. C. Turner, C. Manolatu, B. S. Schmidt, M. Lipson, M. A. Foster, J. E. Sharping, and A. L. Gaeta, Tailored anomalous group-velocity dispersion in silicon channel waveguides, *Opt. Express* **14**, 4357 (2006).
- [56] L.-T. Feng, Y.-J. Cheng, X.-Z. Qi, Z.-Y. Zhou, M. Zhang, D.-X. Dai, G.-C. Guo, and X.-F. Ren, Entanglement generation using cryogenic integrated four-wave mixing, *Optica* **10**, 702 (2023).

- [57] M. Kues, C. Reimer, P. Roztocki, L. R. Cortés, S. Sciara, B. Wetzl, Y. Zhang, A. Cino, S. T. Chu, B. E. Little, D. J. Moss, L. Caspani, J. Azaña, and R. Morandotti, On-chip generation of high-dimensional entangled quantum states and their coherent control, *Nature* **546**, 622 (2017).
- [58] C. Reimer, S. Sciara, P. Roztocki, M. Islam, L. R. Cortés, Y. Zhang, B. Fischer, S. Loranger, R. Kashyap, A. Cino, S. T. Chu, B. E. Little, D. J. Moss, L. Caspani, W. J. Munro, J. Azaña, M. Kues, and R. Morandotti, High-dimensional one-way quantum processing implemented on  $d$ -level cluster states, *Nat. Phys.* **15**, 148 (2019).
- [59] J. Wang, F. Sciarrino, A. Laing, and M. G. Thompson, Integrated photonic quantum technologies, *Nat. Photonics* **14**, 273 (2020).
- [60] Y. Wang, K. D. Jöns, and Z. Sun, Integrated photon-pair sources with nonlinear optics, *Appl. Phys. Rev.* **8**, 011314 (2021).
- [61] E. Pelucchi, G. Fagas, I. Aharonovich, D. Englund, E. Figueroa, Q. Gong, H. Hannes, J. Liu, C.-Y. Lu, N. Matsuda, J.-W. Pan, F. Schreck, F. Sciarrino, C. Silberhorn, J. Wang, and K. D. Jöns, The potential and global outlook of integrated photonics for quantum technologies, *Nat. Rev. Phys.* **4**, 194 (2022).
- [62] W. D. Sacher, T. Barwicz, B. J. F. Taylor, and J. K. S. Poon, Polarization rotator-splitters in standard active silicon photonics platforms, *Opt. Express* **22**, 3777 (2014).
- [63] Z.-S. Hou, X. Xiong, J.-J. Cao, Q.-D. Chen, Z.-N. Tian, X.-F. Ren, and H.-B. Sun, On-chip polarization rotators, *Adv. Opt. Mater.* **7**, 1900129 (2019).
- [64] S. Tanzilli, H. De Riedmatten, W. Tittel, H. Zbinden, P. Baldi, M. De Micheli, D. B. Ostrowsky, and N. Gisin, Highly efficient photon-pair source using periodically poled lithium niobate waveguide, *Electron. Lett.* **37**, 26 (2001).